Ann Nucl Med (2008) 22:549–556
DOI 10.1007/s12149-008-0170-z

ORIGINAL ARTICLE

Three-dimensional SPECT reconstruction with transmission-dependent scatter correction

Antti Sohlberg · Hiroshi Watabe · Hidehiro Iida

Received: 26 March 2007 / Accepted: 8 January 2008

Abstract
Objective The quality of single-photon emission computed tomography (SPECT) imaging is hampered by attenuation, collimator blurring, and scatter. Correction for all of these three factors is required for accurate reconstruction, but unfortunately, reconstruction-based compensation often leads to clinically unacceptable long reconstruction times. Especially, efficient scatter correction has proved to be difficult to achieve. The objective of this article was to extend the well-known transmission-dependent convolution subtraction (TDCS) scatter-correction approach into a rapid reconstruction-based scatter-compensation method and to include it into a fast 3D reconstruction algorithm with attenuation and collimator-blurring corrections.
Methods Ordered subsets expectation maximization algorithm with attenuation, collimator blurring, and accelerated transmission-dependent scatter compensation were implemented. The new reconstruction method was compared with TDCS-based scatter correction and with one other transmission-dependent scatter-correction method using Monte Carlo simulated projection data of ^{99m}Tc-ECD and ^{123}I-FP-CIT brain studies.
Results The new reconstruction-based scatter compensation outperformed the other two scatter-correction methods in terms of quantitative accuracy and contrast measured with normalized mean-squared error, gray-to-white matter and striatum-to-background ratios, and also in visual quality. Highest accuracy was achieved when all the corrections (i.e., attenuation, collimator blurring, and scatter) were applied.
Conclusions The developed 3D reconstruction algorithm with transmission-dependent scatter compensation is a promising alternative to accurate and efficient SPECT reconstruction.

Keywords Statistical reconstruction · Scatter correction · Collimator-blurring correction · Attenuation correction

A. Sohlberg · H. Watabe · H. Iida (✉)
National Cardiovascular Center Research Institute,
5-7-1 Fujishiro-dai, Suita, Osaka 565-8565, Japan
e-mail: iida@ri.ncvc.go.jp

Introduction

The qualitative and quantitative accuracy of single-photon emission computed tomography (SPECT) is hampered by attenuation, collimator blurring, and scatter. Whereas attenuation and collimator blurring can nowadays be corrected in clinically acceptable times, accurate and efficient scatter correction has been proved to be a more difficult problem even though scatter compensation has received a lot of attention over the past two decades.

Scatter-correction methods can generally be divided into two groups: projection- and reconstruction-based methods. In the projection-based methods, scatter correction is usually performed by subtracting the scatter contribution from the projection data before the actual reconstruction [1]. These methods differ in how the scatter contribution is determined. The projection-based methods are usually easy to implement and fast to execute, but the overall improvement in image quality achieved with the scatter compensation, is often reduced by the noise increase in the reconstructed images owing to the subtraction procedure. The reconstruction-based scatter-correction methods, on the other hand, include the effects of scatter into the forward- and backprojec-

tors of the reconstruction algorithm without direct scatter subtraction. The reconstruction-based methods have been shown to achieve greater accuracy and lower noise level than the projection-based methods [2, 3], but they are often unsuitable for clinical practice owing to unacceptably long execution times because scatter calculations have to be repeated at each iteration of the reconstruction algorithm.

One promising projection-based scatter-correction method that has received a lot of attention is the transmission-dependent convolution subtraction (TDCS) algorithm [4]. TDCS has been used by our group to correct scatter in cerebral blood flow [5] and dopamine transporter [6] quantitation studies. Despite the relatively good performance of TDCS in the aforementioned experiments, TDCS is still hampered by the fact that as a projection-based scatter-correction method it relies on scatter subtraction, and also by the fact that it needs geometric mean (GM) projection data, which for example renders accurate collimator-blurring correction impossible.

Even though the traditional TDCS scatter correction has its limitations, the transmission-dependent scatter-modeling approach, when included in reconstruction-based scatter-compensation method, might prove to be useful. Hutton et al. [7, 8] used transmission-dependent scatter modeling to generate scatter projections, which could be included in iterative reconstruction algorithm to perform reconstruction-based scatter compensation in their two-step reconstruction procedure. In this method, Hutton first reconstructed a "scatter-free" image using broad-beam attenuation map. This image was then used as an input for a transmission-dependent scatter-modeling algorithm to calculate scatter projections, which were finally used as a constant additive term in the final "scatter-corrected" reconstruction according to the method of Bowsher and Floyd [9]. The objective of our work was to extend the two-step transmission-dependent scatter correction by Hutton to a "more natural" single-step scatter-compensation method and to include it into a fast 3D reconstruction algorithm with attenuation and collimator-blurring corrections. We also compared our new reconstruction method with Hutton's method and also with conventional TDCS scatter-correction approach in terms of quantitative accuracy, contrast, and image quality.

Materials and methods

Implementation of the reconstruction algorithms

The attenuation, collimator blurring, and scatter correction were implemented into ordered subsets expectation maximization (OSEM) algorithm [10]. The OSEM is given by

$$f_j^{\text{new}} = \frac{f_j^{\text{old}}}{\sum_{i \in S_n} a_{ij}} \sum_{i \in S_n} a_{ij} \frac{p_i}{\sum_k a_{ik} f_k^{\text{old}}}, \quad (1)$$

where f is the reconstructed image, p the measured projections, j (or k) reconstruction voxel index, i projection pixel index, a_{ij} the probability that emission from voxel j is detected in pixel i, and S_n the nth subset. The image update in OSEM consists of sequential forward- and backprojection operations. The estimated projections are obtained by forwardprojecting the current image estimate ($\sum_k a_{ik} f_k^{\text{old}}$) and correction terms that are used to update the old image are formed by backprojecting the ratio of the measured and estimated projections ($\sum_{i \in S_n} a_{ij} \frac{p_i}{\sum_k a_{ik} f_k^{\text{old}}}$).

Here, the forward- and backprojectors were implemented as rotation based [11] (Fig. 1a), which makes attenuation, collimator blurring, and scatter correction relatively straightforward to perform. Attenuation correction factors for each voxel were calculated simply by summing the rotated attenuation map along columns. Collimator blurring, on the other hand, was modeled by convolving each plane of the reconstruction matrix parallel to the projection plane with a collimator response kernel, which was spatially invariant in that plane (Fig. 1b) [12]. The collimator response function was assumed to be a 2D Gaussian function, whose full width at half maximum (FWHM) is linearly dependent on the distance (d_{col}) from the plane to the collimator

$$\text{FWHM}(d_{\text{col}}) = \alpha + \beta d_{\text{col}}. \quad (2)$$

Scatter modeling was implemented by slightly modifying the method presented by Hutton et al. [7, 8]. Hutton's method applies the rotating projectors and it compensates scatter as follows:

1. At each projection angle a "scatter-free" image, which has been obtained with reconstruction of the measured projection data using broad-beam attenuation coefficients, is first multiplied with monoexponential scatter kernel ($e^{-\alpha(d_{\text{tis}})r}$), whose slope ($\alpha$) is dependent on depth (d_{tis}) in tissue. A single scatter kernel is used for each plane at different tissue depth (see Fig. 1b).
2. Each point on each plane is then scaled with a transmission-dependent scatter-to-primary scatter fraction $SF_{S/P}$:

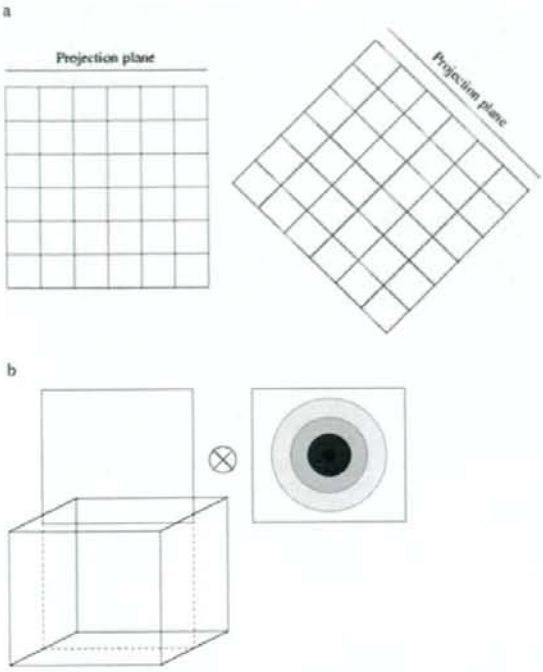

Fig. 1 **a** At each projection angle (two projection angles are shown), the rotating projector rotates the reconstruction matrix (single transverse plane is shown) so that its front face is aligned with the projection plane. The projections can be calculated simply by summing along columns of the reconstruction matrix. **b** Collimator response and scatter response modeling are realized by convolving each plane of the rotated reconstruction matrix (3D view is shown) parallel to the projection plane with an appropriate kernel

$$\mathrm{SF}_{\mathrm{S/P}} = A - B\left[e^{-\sum_{k=j}^{\mathrm{skin}}\mu_k\Delta}\right]^{\gamma} - 1, \tag{3}$$

where A, B, and γ are the coefficients obtained from measurement [4], μ_k is the linear attenuation coefficient for voxel k and Δ voxel size.

3. The convolved and scaled voxel values are finally forwardprojected for obtaining scatter projection for the current projection angle.
4. After all the scatter projections are available, a new reconstruction is started. In this final reconstruction, the scatter projections obtained in the previous step are held as a constant term (s), which is added to the calculated projections $\left(\sum_k a_{ik} f_k^{\mathrm{old}} + s\right)$.

Our new method differs from Hutton's method by the fact that it does not use a pre-reconstructed broad-beam attenuation coefficient image to calculate the scatter projections, but instead we perform the convolution and scatter-fraction scaling using the current image estimate (f_j^{old}). Therefore, our scatter compensation can be presented as

1. In the forwardprojection step of the OSEM algorithm at each projection angle the current image estimate (f_j^{old}) is convolved with the scatter kernels.
2. Each point on each plane is then scaled with the transmission-dependent scatter fraction.
3. The convolved and scaled voxel values are finally forwardprojected and added to the forwardprojected primary counts.

We believe that our approach leads to more natural scatter compensation, reduces user intervention and execution time.

Scatter modeling makes reconstruction time consuming and therefore we used coarse-grid modeling [13] to provide further improvement in speed. In coarse-grid scatter modeling, scatter compensation is performed using larger voxel size than the actual reconstruction voxel size (in our case scatter was calculated using a 64 × 64 × 64 matrix in the case of a 128 × 128 × 128 reconstruction matrix). It is also worth pointing out that our method models scatter only in the forwardprojection step and do not use collimator-blurring compensation in scatter estimation.

The conventional TDCS was implemented according to Meikle et al. [4] using a single exponential convolution kernel and scatter-to-total scatter fractions ($\mathrm{SF}_{\mathrm{S/T}}$)

$$\mathrm{SF}_{\mathrm{S/T}} = \frac{1}{A - Bt_i^{B/2}}, \tag{4}$$

where t_i is transmission factor for projection pixel i. Convolution with the depth-independent scatter kernel ($e^{-\alpha r}$) was performed to the measured projections (p_{meas}) after taking the GM and the result was scaled with the scatter fraction. The resulting scatter projections were subtracted from the measured projections for obtaining "scatter-free" projections (p_{nosc}):

$$p_{\mathrm{nosc}} = p_{\mathrm{meas}} - \mathrm{SF}_{\mathrm{S/T}}(p_{\mathrm{meas}} \otimes e^{-\alpha r}). \tag{5}$$

The scatter-free projections were finally reconstructed using OSEM.

Reconstruction al gorithm calibration

The parameters needed for collimator blurring and scatter correction were obtained from Monte Carlo simulations with the SIMIND simulator [14]. A low-energy

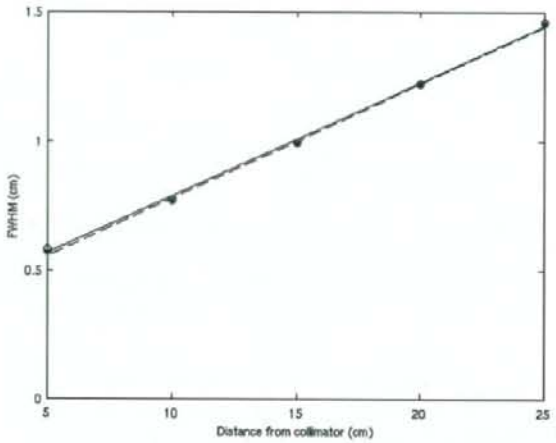

Fig. 2 Full width at half maximum as a function of distance from the collimator for ^{99m}Tc and ^{123}I. ^{99m}Tc measurements are shown with *circles* and the linear model fit (Eq. 2) as *solid line*, whereas ^{123}I measurements are presented with *stars* and the linear model fit as *dashed line*. The parameters α and β in Eq. 2 for ^{99m}Tc were 0.35 and 0.04 and for ^{123}I 0.33 and 0.04, respectively

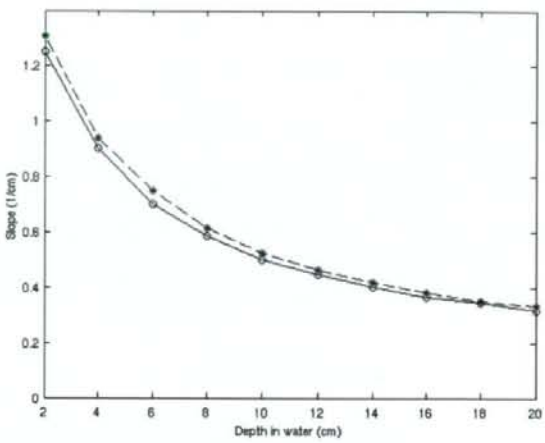

Fig. 3 Scatter kernel slope as a function of depth in water for ^{99m}Tc and ^{123}I. ^{99m}Tc measurements are shown with *solid line* with *circles* and ^{123}I measurements using *dashed line* with *stars*

high-resolution parallel hole collimator with 0.14 cm in hole diameter, a hole length of 2.7 cm, and a septal thickness of 0.018 cm was used. The pixel size in the simulations was set to 0.2 cm, and the projection data were acquired into a 128 × 128 matrix. Two sets of simulations were performed using ^{99m}Tc and ^{123}I as radionuclides. Symmetrical 15% energy window was centered on the photo-peak. For ^{123}I high-energy photons were not included in the simulations.

The FWHM as a function of distance was obtained by simulating point sources in air at different distances (5 cm, 10 cm, 15 cm, 20 cm, and 25 cm) from the collimator. FWHM was calculated by fitting a Gaussian function to a profile drawn through the center of the image, and the intercept (α) and slope (β) in Eq. 2 were obtained by fitting the linear model to the measurements (see Fig. 2).

The scatter kernel slope [$\alpha(d_{tis})$] for the reconstruction-based scatter-correction methods (Hutton's method and new method) was obtained by simulating a line source behind slabs of different thickness (2 cm, 4 cm, 6 cm, 8 cm, 10 cm, 12 cm, 14 cm, 16 cm, 18 cm, and 20 cm) of water. Low noise level planar images of the line sources were acquired and the slopes were calculated by fitting exponential functions to the scatter tails of profiles drawn through the center of the image. The results of this experiment are presented in Fig. 3. The slope for each plane at different depths in tissue in the reconstruction-based scatter correction was obtained by linear interpolation from the measurements. The slope for depth-independent scatter kernel in the conventional TDCS was set to 0.45 l/cm for ^{99m}Tc and 0.47 1/cm for ^{123}I.

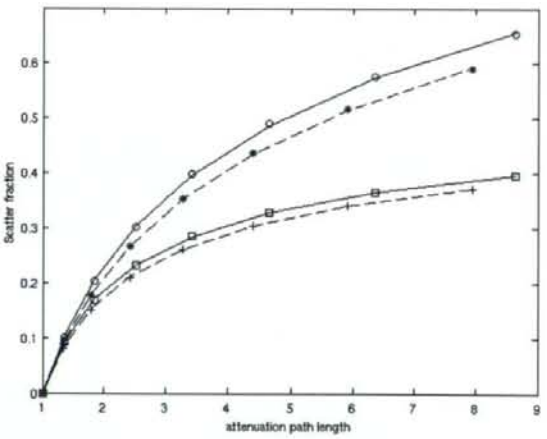

Fig. 4 Scatter fractions as a function of attenuation path length for ^{99m}Tc and ^{123}I. Scatter-to-primary ^{99m}Tc measurements are shown with *circles*, scatter-to-primary ^{123}I measurements with *stars*, scatter-to-total ^{99m}Tc measurements with *squares*, and scatter-to-total ^{123}I measurements are presented with plusses. The build-up equation fit (Eqs. 3, 4) for ^{99m}Tc is shown with *solid line* and for ^{123}I as *dashed line*. The build-up equation parameters *A*, *B*, and γ were 3.6, 2.6, and 0.13 for ^{99m}Tc and 4.3, 3.3, and 0.09 for ^{123}I. The same *A*, *B*, and γ parameters fitted well in both Eqs. 3 and 4

The *A*, *B*, and γ scatter-fraction coefficients were calculated by simulating point sources behind slabs of different thicknesses (2 cm, 4 cm, 6 cm, 8 cm, 10 cm, 12 cm, and 14 cm) of water. The scatter fractions were obtained from SIMIND, and these measurements were

fitted to Eqs. 3 and 4. Results from this experiment are presented in Fig. 4.

Brain phantom simulations

The new reconstruction-based scatter-correction method was compared with that of Hutton's method and to TDCS using the Zubal brain phantom [15]. The phantom was modified to represent the uptake of ^{99m}Tc-ECD (gray-to-white matter ratio 2.5:1) and ^{123}I-FP-CIT (striatum-to-background ratio 4:1). SIMIND was used to create low noise projection data of the phantoms, 120 angles over 360° circular orbit, by simulating approximately 70 MCts/projection using the same parameters as was used in determining the parameters for the reconstruction algorithms with the exception that pixel size was now 0.225 cm. Attenuation map was created by assigning correct densities for brain tissue and skull. The low-noise projections were then used to create noisy projection sets containing a total of 5 MCts for the ^{99m}Tc-ECD and 2 MCts for the ^{123}I-FP-CIT, which represent the average total count levels of ^{99m}Tc-ECD and ^{123}I-FP-CIT in clinical studies (personal communication Prof. Jyrki T. Kuikka, Kuopio University Hospital, Finland).

The noisy projection data were reconstructed using the new algorithm with (4 iterations and 15 subsets) and without collimator modeling (2 iterations and 15 subsets) and the GM projections with/without TDCS (2 iterations and 10 subsets). Reconstructions with collimator modeling used more iterations because of their slower convergence. Both reconstructions according to Hutton's method were performed with 2 iterations and 15 subsets. All the reconstructed images were post-filtered using a 3D Butterworth filter (cut-off 1.0 cycles/cm, order 5) according to clinical practice. The accuracy of the reconstruction methods was studied by comparing the overall accuracy of the reconstruction and correction methods and by calculating the normalized mean-squared error (NMSE) with respect to the known true counts (f_j^{true}):

$$\text{NMSE} = \frac{\sum_j \left(f_j^{\text{true}} - f_j\right)^2}{\sum_j f_j^{\text{true}^2}} \tag{6}$$

and the average gray-to-white matter and striatum-to-background ratios.

Results

Results of the Zubal brain phantom experiments are shown in Table 1. As can be seen, the reconstruction-based scatter-correction methods outperform the conventional TDCS in terms of contrast (gray-to-white matter and striatum-to-background ratios) and quantitative accuracy (normalized mean-squared errors). The new method is more accurate than that of Hutton's one, but the difference between the two is small. Highest accuracy is achieved when collimator-blurring correction is also applied during reconstruction. Indeed, collimator-blurring compensation might prove to be very useful in quantitative brain studies because it clearly reduces the partial volume effect offering higher accuracy. Interestingly, reconstructions from GM projections with only attenuation correction perform worse than reconstructions from normal projections. This is primarily caused by differences in attenuation correction. GM projections require projection space attenuation correction, whereas more accurate reconstruction space attenuation correction can be performed with normal projections. Examples of images with different reconstruction methods are shown in Figs. 5 and 6. The reconstruction-based scatter-compensation methods provide slightly better image quality than TDCS and the best result is obtained when collimator-blurring correction is also applied.

Table 1 Normalized mean-squared error (NMSE), gray-to-white matter ratio (GM:WM), and striatum-to-background ratio (STR:BG) for the ^{99m}Tc-ECD and ^{123}I-FP-CIT simulation studies

Corrections	NMSE_{ECD}	GM:WM	$\text{NMSE}_{\text{FP-CIT}}$	STR:BG
Attenuation*	0.186/0.182	1.11/1.17	0.136/0.134	2.19/2.24
Attenuation + $\text{scatter}_{\text{TDCS}}$	0.179	1.15	0.134	2.27
Attenuation + $\text{scatter}_{\text{Hutton}}$	0.173	1.24	0.127	2.29
Attenuation + $\text{scatter}_{\text{New}}$	0.172	1.25	0.126	2.29
Attenuation + $\text{scatter}_{\text{New}}$ + CDR	0.165	1.41	0.121	2.48

Results are presented for ordered subsets expectation maximization (OSEM) reconstruction with only attenuation correction, with attenuation and scatter correction [transmission-dependent convolution subtraction (TDCS)-based, Hutton's method and new method] and with attenuation, new scatter, and collimator-blurring correction (CDR). The attenuation correction only results are presented for two algorithms: geometric mean (GM) projection OSEM reconstruction, which has to be used for TDCS-based scatter correction and normal OSEM reconstruction which is used for Hutton's and new scatter-compensation methods

*The first values shown are the results of GM projection reconstruction and the second the results of normal reconstruction

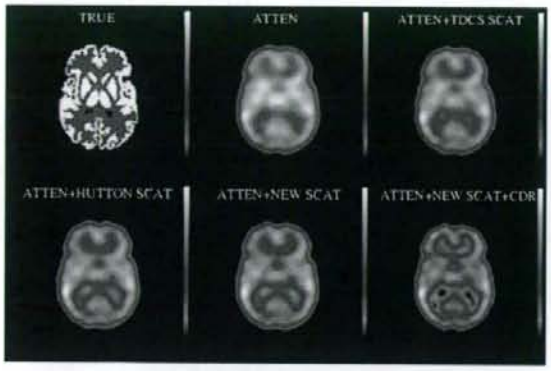

Fig. 5 Representative slices of the ^{99m}Tc-ECD study obtained with ordered subsets expectation maximization (OSEM) using only attenuation correction (reconstruction with normal projections), attenuation + transmission-dependent convolution subtraction (TDCS)-based scatter correction, attenuation + Hutton's scatter correction, attenuation + new scatter correction, and attenuation + new scatter + collimator-blurring (CDR) correction

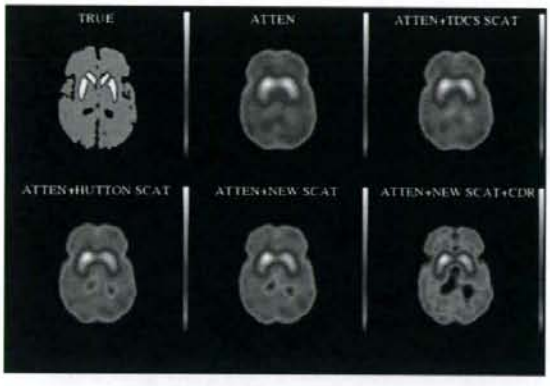

Fig. 6 Representative slices of the ^{123}I-FP-CIT study obtained with OSEM using only attenuation correction (reconstruction with normal projections), attenuation + TDCS-based scatter correction, attenuation + Hutton's scatter correction, attenuation + new scatter correction, and attenuation + new scatter + CDR correction

The average reconstruction times of the ^{99m}Tc-ECD and ^{123}I-FP-CIT Zubal phantom experiments are listed in Table 2. The TDCS is much faster than other methods, but it is worth noting that because of the GM projections TDCS uses only 60 projections in reconstruction, whereas the new method uses 120 projection images. TDCS also applies projection-based attenuation modeling as explained earlier, and therefore it does not require rotation of the attenuation map during the reconstruction, which saves time. Hutton's method is by far the slowest one because it requires pre-reconstruction to calculate scatter projections, but when the scatter projections are ready the actual scatter correction in the final reconstruction is faster than scatter compensation with the new method.

Table 2 Average reconstruction times for the ^{99m}Tc-ECD and ^{123}I-FP-CIT studies

Corrections	Time per iteration (s)
Attenuation[a]	67/212
Attenuation + scatter$_{TDCS}$	67
Attenuation + scatter$_{Hutton}$[b]	560 + 212
Attenuation + scatter$_{New}$	254
Attenuation + scatter$_{New}$ + CDR	336

Results are presented for OSEM reconstruction with only attenuation correction, with attenuation and scatter correction (TDCS-based, Hutton's method and new method) and with attenuation, new scatter, and collimator-blurring correction (CDR). The attenuation correction only results are presented for two algorithms: geometric mean (GM) projection OSEM reconstruction, which has to be used for TDCS-based scatter correction and normal OSEM reconstruction which is used for Hutton's and new scatter-compensation method. Calculation times have been obtained using 1.7 GHz Pentium processor with 1 GB RAM

[a] The first value shown is the time for GM projection reconstruction and the second is for normal reconstruction

[b] Pre-reconstruction and scatter forwardprojection calculation time + time for single iteration for the final reconstruction

Discussion

Here, we implemented a 3D reconstruction algorithm with transmission-dependent scatter modeling for efficient reconstruction-based scatter correction and compared it with reconstruction-based scatter-compensation method presented by Hutton et al. [7, 8], and with the conventional TDCS-based scatter-correction method [4]. The new algorithm proved to provide the highest accuracy according to Monte Carlo simulation studies of Zubal brain phantom (see Table 1). The new algorithm is also very advantageous because it allows easy incorporation of accurate attenuation and collimator-blurring corrections, which might prove to be very useful in high-quality SPECT imaging.

The presented scatter-correction method is relatively easy to implement and use. It requires two measurements for calibration: line source measurement to determine the scatter kernel slopes and point source measurement to determine the scatter fractions. These measurements need to be performed once for each radionuclide and collimator pair. In fact for lower-energy isotopes such as ^{99m}Tc, the scatter fractions have shown to be collimator independent [16] and therefore a single measurement might be sufficient for scatter-correction calibration for a large family of different collimators.

In addition to the ease of implementation, the execution time is of importance if a reconstruction method is to be used in clinical practice. Table 2 lists the calculation times per iteration for the scatter-correction methods. The TDCS-based scatter correction is clearly the fastest method, but the new method does not provide an extensive increase in computation time when compared with reconstruction without scatter correction. It is worth pointing out that even though the new method was accelerated using the coarse-grid scatter modeling, the reconstruction algorithm itself is not yet fully optimized. We believe that by further optimizing the structure of our reconstruction code and by replacing the current bilinear interpolation-based reconstruction grid rotation with a faster three-pass shear [17] method, we can still greatly reduce the computation time from the current 336 s/iteration.

This study has some limitations. First, testing and comparison of algorithms was performed using simplified simulated data. Simulated data were chosen, because they allowed easy comparison with true activity distributions, which are beneficial to finding small errors in initial reconstruction experiments. Simulations were performed as Monte Carlo simulations, which are known to have relatively good correspondence with real clinical data and we also tried to closely mimic clinical-imaging situations using appropriate noise levels and post-filters. On the other hand, it should be realized that even Monte Carlo simulations will probably produce results that are too good owing to the absence of errors in energy window calibration, non-uniformities, and so on that often hamper the quality of clinical data. Moreover, the high-energy photons of ^{123}I, which can penetrate or scatter at the collimator, were not included in the simulations, and the reconstructions were performed with noise-free and perfectly aligned attenuation maps. Both of these conditions are unnatural and their effects have to be investigated in detail in further studies.

Second, the metrics (NMSE and activity ratios) that were used to analyze the reconstructed images are simplistic, and more clinically relevant measures such as cerebral blood flow, binding potential, or task-based measures such as lesion detection are required in future studies to evaluate the true benefits of the presented reconstruction and corrections methods. Comparison of the new transmission-dependent scatter correction with other reconstruction-based scatter-correction methods such as in Beekman et al. [18] and Frey et al. [19] would also make an interesting topic for a further investigation.

In summary, we have proposed a 3D reconstruction algorithm with attenuation, collimator blurring, and transmission-dependent scatter correction, which shows promise as an efficient and accurate reconstruction method; however, further testing is still required to evaluate its true applicability in the clinical setting.

Acknowledgment This work was supported by grants from the Japan Society for the Promotion of Science.

References

1. Buvat I, Rodriguez-Villafuerte M, Todd-Pokropek A, Benali H, Di Paola R. Comparative assessment of nine scatter correction methods based on spectral analysis using Monte Carlo simulations. J Nucl Med 1995;36:1476–88.
2. Frey EC, Tsui BMW, Ljungberg M. A comparison of scatter compensation methods in SPECT: subtraction-based techniques versus iterative reconstruction with accurate modeling of the scatter response. Conference Record of the 1992 Nuclear Science Symposium and Medical Imaging Conference 1992;2: 1035–7.
3. Beekman FJ, Kamphuis C, Frey EC. Scatter compensation methods in 3D iterative reconstruction: a simulation study. Phys Med Biol 1997;42:1619–32.
4. Meikle SR, Hutton BF, Bailey DL. A transmission-dependent method for scatter correction in SPECT. J Nucl Med 1994; 35:360–7.
5. Iida H, Narita Y, Kado H, Kashikura A, Sugawara S, Shoji Y, et al. Effects of scatter and attenuation correction on quantitative assessment of regional cerebral blood flow with SPECT. J Nucl Med 1998;39:181–9.
6. Kim KM, Varrone A, Watabe H, Shidahara M, Fujita M, Innis RB, et al. Contribution of scatter and attenuation compensation to SPECT images of nonuniformly distributed brain activities. J Nucl Med 2003;44:512–9.
7. Hutton BF, Osiecki A, Meikle SR. Transmission-based scatter correction of 180° myocardial single-photon emission tomographic studies. Eur J Nucl Med 1996;23:1300–8.
8. Hutton BF, Baccarne V. Efficient scatter modelling for incorporation in maximum likelihood reconstruction. Eur J Nucl Med 1998;25:1658–65.
9. Bowsher JE, Floyd CE. Treatment of Compton scattering in maximum-likelihood expectation maximization reconstructions of SPECT images. J Nucl Med 1991;32:1285–91.
10. Hudson HM, Larkin RS. Accelerated image reconstruction using ordered subsets of projection data. IEEE Trans Med Imaging 1994;13:601–9.
11. Zeng GL, Gullberg GT. Frequency domain implementation of the three-dimensional geometric point response correction in SPECT imaging. IEEE Trans Nucl Sci 1992;39:1444–53.
12. Zeng GL, Gullberg GT, Bai C, Christian PE, Trisjono F, Di Bella EVR, et al. Iterative reconstruction of fluorine-18 SPECT using geometric point response correction. J Nucl Med 1998; 39:124–30.
13. Kadrmas DJ, Frey EC, Karimi SS, Tsui BMW. Fast implementations of reconstruction-based scatter compensation in fully 3D SPECT image reconstruction. Phys Med Biol 1998;43: 857–73.
14. Ljungberg M, Strand SE. A Monte Carlo program for the simulation of scintillation camera characteristics. Comput Methods Programs Biomed 1989;29:257–72.
15. Zubal IG, Harrell CR, Smith EO, Rattner Z, Gindi G, Hoffer PB. Computerized three-dimensional segmented human anatomy. Med Phys 1994;21:299–302.

16. Kim KM, Watabe H, Shidahara M, Ishida Y, Iida H. SPECT collimator dependency of scatter and validation of transmission-dependent scatter compensation methodologies. IEEE Trans Nucl Sci 2001;48:689–96.
17. Di Bella EVR, Barclay AB, Eisner RL, Schafer RW. A comparison of rotation-based methods for iterative reconstruction algorithms. IEEE Trans Nucl Sci 1996;43:3370–6.
18. Beekman FJ, de Jong HW, van Geloven S. Efficient fully 3-D iterative SPECT reconstruction with Monte Carlo-based scatter compensation. IEEE Trans Med Imaging 2002;21: 867–77.
19. Frey EC, Ju ZW, Tsui BMW. A fast projector-backprojector pair modeling the asymmetric, spatially varying scatter response function for scatter compensation in SPECT imaging. IEEE Trans Nucl Sci 1993;40:1192–7.

Heart and Brain Circulation and CO2 in Healthy Men

Ikuo Yokoyama M.D.[a,c], Yusuke Inoue M.D.[b] ,Toshibumi Kinoshita M.D.[c], Hiroshi Itoh M.D.[c,d], Iwao Kanno,[c,d], Hidehiro Iida PhD., Dsc [d, e]

[a] Department of Cardiovascular Medicine, Sanno Hospital, International University of Health and Welfare, Tokyo, Japan, [b] Department of Radiology, Institute of Medical Science, Graduate School of Medicine University of Tokyo, Tokyo, Japan, [c] Department of Radiology Akita Research Institute of Brain and Blood Vessels, Akita, Japan, [d] Brain Imaging Project, National Institute of Radiological Sciences, [e] Department of Radiology, the Research Institute of National Cardiovascular Center, Osaka, Japan.

Address for correspondence;

Ikuo Yokoyama M.D.

Correspondence to: Dr Ikuo Yokoyama, Department of Cardiovascular Medicine, Sanno Hospital, International University of Health and Welfare, 8-10-16 Akasaka, Minato-ku, Tokyo 107-0052, Japan

TEL: +81-3-3402-3151

FAX: +81-3-3404-3652

E-mail: yokochan-tky@umin.ac.jp

Received: 21/10/07

Revision Requested: 3/12/2007

Revision Received: 1/2/2008

Accepted: 8/2/2008

Short title: Heart and Brain Perfusion and CO2

This is an Accepted Work that has been peer-reviewed and approved for publication in the *Acta Physiologica*, but has yet to undergo copy-editing and proof correction. See http://www.blackwell-synergy.com/loi/aps for details. Please cite this article as a "Postprint"; doi: 10.1111/j.1748-1716.2008.01846.x

Abstract

Aim: To compare blood flow response to arterial carbon dioxide tension change in the heart and brain of normal elderly men.

Methods: Thirteen healthy elderly male volunteers were studied. Hypercapnea was induced by carbon dioxide inhalation and hypocapnea was induced by hyperventilation. Myocardial blood flow ($mL \cdot minute^{-1} \cdot [100\ gram\ of\ perfusable\ tissue]^{-1}$) and cerebral blood flow ($mL \cdot minute^{-1} \cdot [100\ gram\ of\ perfusable\ tissue]^{-1}$) were measured simultaneously at rest, under carbon-dioxide gas inhalation and hyperventilation using the combination of two positron emission tomography scanners.

Results: Arterial carbon dioxide tension increased significantly during carbon dioxide inhalation (43.1±2.7 mmHg, $p < 0.05$) and decreased significantly during hyperventilation (29.2±3.4 mmHg, $p< 0.01$) from baseline (40.2±2.4 mmHg). Myocardial blood flow increased significantly during hypercapnea (88.7±22.4, $p < 0.01$) from baseline (78.2±12.6), as did the cerebral blood flow (baseline: 39.8±5.3 vs. hypercapnea: 48.4±10.4, $p < 0.05$). During hypocapnea cerebral blood flow decreased significantly (27.0±6.3, $p < 0.01$) from baseline as did the myocardial blood flow (55.1±14.6, $p < 0.01$). However normalized myocardial blood flow by cardiac workload ($100mL \cdot mmHg^{-1} \cdot [heart\text{-}beat]^{-1} \cdot [gram\ of\ perfusable\ tissue]^{-1}$) was not changed from baseline (93.4±16.6) during hypercapnea (90.5±14.3) but decreased significantly from baseline during hypocapnea (64.5±18.3, $p < 0.01$).

Conclusion: In normal elderly men, hypocapnea produces similar vasoconstriction in both heart and brain. Mild hpercapnea increased cerebral blood flow but did not have an additional effect to dilate coronary arteries beyond the expected range in response to an increase in cardiac workload.

Key Words: Carbon dioxide, Coronary circulation, Cerebrovascular circulation, Hypercapnea, Hyperventilation, Hypocapnea, Myocardial blood flow, Positron emission tomography

Introduction

Correlation between arterial carbon dioxide tension and cerebral blood flow is well established [Kety & Schmidt 1948, Shimosegawa et al. 1995, Kuwabara et al. 1997]. However, responsiveness of myocardial blood flow to hypercapnea and hypocapnea has not been fully elucidated. These relationships were investigated in animal experiments [Feinberg et al. 1960, Love et al. 1965, Case & Greenberg 1976, Bos et al. 1979, Powers et al. 1986] and human clinical studies [Rowe et al. 1962, Neill & Hattenhauer 1975, Wilson et al. 1981, Kazmaier et al. 1998] with conflicting results. The inconsistencies observed should be attributable to differences in experimental conditions, such as the techniques used for measurement, or whether the studies were performed in animals or humans, or presence versus absence of ischemic heart disease.

In this study, we evaluated the responses of myocardial blood flow and cerebral blood flow to hypercapnea and hypocapnea in healthy elderly men. We employed a dual positron emission tomography (PET) scanner consisting of two scanners to measure myocardial blood flow and cerebral blood flow simultaneously in the same subject [Iida et al. 1998]. PET allows assessment of functional parameters under physiological conditions. Using this dual PET scan technique allowed simultaneous assessment of myocardial and cerebral circulations, noninvasively and reliably and enabled comparison of the two.

Materials and Methods

Study Subjects

Thirteen healthy men (age range 51-71 years; mean 59.4, standard deviation [5.5]) who had been the subjects of previously published studies with different objectives [Iida et al. 1998, Ito et al. 1999, Ito et al. 2000, Ito et al. 2002] took part in the study. These men had normal laboratory parameters, no signs or symptoms of ischemia in the heart or brain, and no abnormalities were found by brain magnetic resonance imaging, electrocardiography, cardiac echocardiography, and physical examination. All subjects provided written informed consent that data obtained from the PET studies could be used for research purposes. The study protocol was approved by the Ethics Committee of the Research Institute of Brain and Blood Vessels, Akita, Japan.

PET Procedures

The Headtome V dual PET system (Shimadzu Corp., Kyoto, Japan), a combination of the two Headtome V PET scanners, was used for all studies [Iida et al. 1998]. The system allowed simultaneous imaging of the brain and heart and provided 47 sections for the brain and 31 sections for the heart with center-to-center distances of 3.125 mm. The intrinsic spatial resolution was 4.0 mm in-plane and 4.3 mm full-width at half-maximum axially. All PET data were acquired in 2D mode and reconstructed with a Butterworth filter, resulting in a final in-plane resolution of approximately 8 mm full-width at half-maximum.

After an overnight fast, subjects were placed in the supine position on the scanner bed. The blood-pool images were obtained 1 minute after continuous inhalation of ^{15}O-CO gas (approximately 5 GBq total applied to the mouth). One minute after the end of ^{15}O-CO gas inhalation, ^{15}O-CO blood-pool images of the heart were obtained with an R-wave triggered electrocardiogram gated tomographic scan. A simultaneous gated static scan on both the heart and brain was done 4 minutes after the inhalation of ^{15}O-CO gas. Three venous blood samples were taken during the ^{15}O-CO scan, and the radioactivity concentration in the whole blood was measured using a NaI-well counter that was cross-calibrated with the PET scanner. ^{15}O-CO blood-pool images were used to draw regions of interests on left ventricular cavity and left ventricular wall accurately to obtain time activity curves. The recovery of

coefficient of left ventricular cavity was given by the myocardial static blood volume image and was also used to determine myocardial blood flow [Iida et al. 1998]. After 12-15 minutes, to allow for decay of ^{15}O-radioactivity to background levels, transmission scanning was undertaken over 10 minutes. Then, $H_2{}^{15}O$ PET studies were performed at rest, and under hypercapnea and hypocapnea. The order of the studies was rest, hypercapnea, and hypocapnea studies in 7 subjects, and rest, hypocapnea, and hypercapnea studies in 6 subjects. The intervals between $H_2{}^{15}O$ PET studies were at least 15 minutes to allow the decay of radioactivity. Following the continuous intravenous infusion of $H_2{}^{15}O$ (1.1-1.4 GBq) over 2 minutes, 180-sec static imaging of the brain and 360-sec dynamic imaging of the heart were commenced. The dynamic data of the heart consisted of twelve 5- seconds frames, eight 15-seconds frames, and six 30- seconds frames. Hypercapnea was achieved by inhalation of 7% CO_2 gas, beginning 1 minute before ^{15}O-water injection and continuing until the end of the imaging of the heart. Hypocapnea was induced by hyperventilation. Three arterial blood samples were taken during each PET scan to measure arterial carbon dioxide tension and pH.

Data Analysis

Cerebral blood flow images were generated from the PET data as described previously [Iida et al. 1998], and a region of interest for the inside of the brain contour was drawn on a slice of the cerebral blood flow image that was at the level of the basal ganglia. The region of interest was determined on an image obtained at rest and applied to images obtained under stress conditions. The mean cerebral blood flow in the region of interest was calculated from ^{15}O-H_2O autoradiography method [Raichle ME et al. 1983] and used for the following analyses. The percent change in cerebral blood flow at hypercapnea was defined as 100 × (cerebral blood flow at hypercapnea - cerebral blood flow at rest) / cerebral blood flow at rest, and cerebral blood flow responsiveness to hypercapnea was calculated as percent change in cerebral blood flow at hypercapnea divided by arterial carbon dioxide tension at hypercapnea minus arterial carbon dioxide tension at rest. The percent change in cerebral blood flow at hypocapnea and cerebral blood flow responsiveness to hypocapnea were determined using similar calculations, but using hypocapnea values instead.

The region of interests for the left ventricular cavity and the whole anterolateral wall

of the left ventricle at mid ventricular level were drawn on a slice of the short-axis myocardial images. The region of interests for the image at rest were copied on the myocardial images under the stress conditions. The myocardial blood flow value was estimated using the regions of interests according to a previously validated method [Iida et al. 1998]. In summary, myocardial blood flow was calculated using a non-linear least squares fitting technique of the left ventricular tissue and arterial ^{15}O-H_2O time activity curves [Iida H et al. 1988]. The input function was non-invasively determined from the time activity curve of left ventricular cavity [Iida H et al. 1992]. Time activity curve of the left ventricular cavity and that of the myocardial wall were fitted to the previously demonstrated tracer kinetic model equations to determine myocardial blood flow [Iida et al. 1998]. The percent change in myocardial blood flow at hypercapnea was defined as 100 × (myocardial blood flow during hypercapnea - myocardial blood flow at rest) / myocardial blood flow at rest, and myocardial blood flow responsiveness to hypercapnea was calculated as percent change in myocardial blood flow during hypercapnea divided by arterial carbon dioxide tension under hypercapnea minus arterial carbon dioxide tension at rest. The percent change in myocardial blood flow during hypocapnea and myocardial blood flow responsiveness to hypocapnea were determined using similar calculations but using hypocapnea values instead. In addition, normalized myocardial blood flow was calculated for the rate pressure product by the equation:

Normalized myocardial blood flow = 10000 × myocardial blood flow / rate pressure product, and percent change in normalized myocardial blood flow and normalized myocardial blood flow responsiveness were calculated.

Statistical Analysis

Values were expressed as the mean ± standard deviation. Comparisons were made by one-way analysis of variance followed by Fisher's least significant difference tests for parametric distributions and Kruskal-Wallis test followed by Scheffe's test for nonparametric distributions. A P value < 0.05 was considered statistically significant.

Results

Hemodynamics

Blood pressures, heart rate, rate pressure product, arterial carbon dioxide tension and pH are summarized in Table 1. Blood pressures were measured in the thigh because arteries and veins in both arms were cannulated. Since the blood pressure measured in the thighs were on average 25 mmHg higher than those measured in the arms in our institution, blood pressures in the thigh were considered to be within normal range. Electrocardiogram findings under hypercapnea or hypocapnea did not change compared with those at rest. Arterial carbon dioxide tension significantly decreased during hypocapnea and significantly increased during hypercapnea. Blood pressures significantly increased during hypercapnea but remained unchanged during hypocapnea. Rate pressure product did not change significantly during hypocapnea but significantly increased during hypercapnea.

Cerebral blood flow

Cerebral blood flow significantly decreased during hypocapnea and significantly increased during hypercapnea (Table2). The change in cerebral blood flow caused by hypocapnea was -32.2 percent ± 11.3 percent, and the cerebral blood flow responsiveness to hypocapnea was 3.0 ± 1.1 percent /mmHg. The change in cerebral blood flow caused by hypercapnea was 21.0 percent ± 15.5 percent, and the cerebral blood flow responsiveness to hypercapnea was 8.2 ± 5.3 percent /mmHg.

Myocardial blood flow

Hypocapnea caused a significant reduction in myocardial blood flow from baseline (Table 2). The percent change in myocardial blood flow caused by hypocapnea was -29.3 percent ± 15.1 percent, and the myocardial blood flow responsiveness to hypocapnea was 3.5 ± 3.0 percent /mmHg. Normalization for rate pressure product did not alter the percent change (- 30.4 percent ± 16.5 percent) and responsiveness (-2.2 ± 11.2 percent /mmHg) substantially. Under hypocapnea, the percent changes in cerebral blood flow, myocardial blood flow, and normalized myocardial blood flow were not significantly different compared with baseline. There were no significant differences in the responsiveness to hypocapnea between cerebral blood flow, myocardial blood flow, and normalized myocardial blood flow.

Hypercapnea significantly increased myocardial blood flow. The percent change in myocardial blood flow caused by hypercapnea was 12.5 percent ± 15.6 percent, and the myocardial blood flow responsiveness to hypercapnea was 5.2 ± 9.9 percent /mmHg. However, the increase in myocardial blood flow disappeared after normalization for rate pressure product. The change in normalized myocardial blood flow under hypercapnea was -2.2 percent ± 11.2 percent, and the normalized myocardial blood flow responsiveness to hypercapnea was -1.7 ± 8.8 percent /mmHg. As for hypercapnea, the percent change in normalized myocardial blood flow was significantly smaller than the change in cerebral blood flow ($p < 0.05$), and the normalized myocardial blood flow responsiveness was significantly smaller than cerebral blood flow responsiveness ($p < 0.05$).

Discussion

We simultaneously measured myocardial blood flow and cerebral blood flow at rest, during hypocapnea, and during hypercapnea in healthy elderly men. During hypocapnea, cerebral blood flow was reduced significantly as expected, and myocardial blood flow also diminished significantly to a similar magnitude. Rate pressure product did not change significantly from baseline, and myocardial blood flow normalized for rate pressure product also decreased. These results indicate that hypocapnea depresses myocardial blood flow, independently of cardiac workload, in healthy elderly men. The responsiveness to hypocapnea was similar between cerebral blood flow and myocardial blood flow, suggesting that hypocapnea can induce vasoconstriction in both heart and brain in healthy elderly men.

Several studies of coronary vascular response to hypocapnea using experimental animals have been reported however, the results were inconsistent [Feinberg 1960, Love 1965, Case 1976]. In a study of humans **with** negligible coronary artery disease, hypocapnea with 30.6 percent reduction in arterial carbon dioxide tension resulted in a significant 30.3 percent reduction in myocardial blood flow with a wide range of variability [Rowe 1962]. The present results are consistent with these previous studies. However, in studies of patients with coronary artery disease, hypocapnea resulted in a mild but significant 12 percent reduction in myocardial blood flow [Neill & Hattenhauer 1975] or did not change significantly [Wilson et al. 1981, Kazmaier et al. 1998]. Therefore, myocardial blood flow response to hypocapnea is likely to be different between normal subjects and patients with coronary artery disease. Since myocardial blood flow response to hypocapnea did not differentiate regions with myocardial ischemia from regions of non-ischemic myocardium in these studies of coronary artery disease, further study is required to clarify whether myocardial blood flow response to hypocapnea would differ between ischemic myocardium and non-ischemic myocardium.

Myocardial blood flow response to hypercapnea remains controversial. A number of experimental animal studies showed that hypercapnea did not increase myocardial blood flow [Feinberg et al. 1960, Love et al. 1965, van den Bos et al. 1979], whereas other studies showed that hypercapnea could increase myocardial blood flow [Case & Greenberg 1975, Powers et al. 1986]. In a study of anesthetized patients with coronary artery disease before

surgery, elevation of arterial carbon dioxide tension (+10 mmHg) resulted in a 15 percent increase in myocardial blood flow [Kazmaier et al. 1998]. However, the study did not estimate normalized myocardial blood flow to exclude the influence of cardiac workload on myocardial blood flow measurement [Kazmaier et al. 1998]. In this study, hypercapnea significantly increased myocardial blood flow and cerebral blood flow but not normalized myocardial blood flow with rate pressure product in healthy elderly men. Myocardial blood flow responsiveness to hypercapnea was significantly lower than that in cerebral blood flow when myocardial blood flow was normalized with respect to rate pressure product. Increase in cardiac workload under hypercapnea could explain an increase in myocardial blood flow. However, hypercapnea did not have an additional direct effect to increase myocardial blood flow independent of an elevation in cardiac workload under mild hypercapnea. Since myocardial blood flow responsiveness to hypercapnea was significantly lower than that in cerebral blood flow when myocardial blood flow was normalized with respect to cardiac workload, vascular responsiveness to hypercapnea is expected to be different between heart and brain. In this study, the magnitude of increase in arterial carbon dioxide tension during hypercapnea was small (3 mmHg), contrasting with the magnitude of decrease in arterial carbon dioxide tension during hypocapnea (11 mmHg). Such difference in the magnitude of changes in arterial carbon dioxide tension may explain why hypocapnea was effective to decrease the normalized myocardial blood flow but hypercapnea had no effect to increase the normalized myocardial blood flow. However, even under such very small increase in carbon dioxide tension, significantly elevated myocardial blood flow without normalization in response to an increase in cardiac workload was seen. Therefore, the importance of the carbon dioxide tension changes in determining the response of heart and brain perfusion could be discussed more than is presently done. To resolve such issues, much stronger hypercapneic stress test at different hypercapnic levels to increase arterial carbon dioxide tension is required to clarify whether hypercapnea directly increases myocardial blood flow independent of an increase in cardiac workload. Use of beta-blockers to exclude an influence of increase in cardiac workload for the myocardial blood flow measurement during hypercapnea [van den Bos et al. 1979, Powers et al. 1986] would also be helpful to understand myocardial blood

flow responsiveness to hypercapnea. For future studies, it is of interest to test the effect of normalization with both cardiac workload and arterial carbon dioxide tension changes on the studies of myocardial blood flow.

Conclusion

In normal elderly men, hypocapnea produces similar vasoconstriction in both heart and brain. Mild hpercapnea increased cerebral blood flow but did not have an additional effect to dilate coronary arteries beyond the expected range in response to an increase in cardiac workload.

ACKNOWLEDGMENTS

This work was supported by grants from the Research Institute of Brain and Blood Vessels, Akita, Japan. We are grateful to Dr. T. Komaru (Tohoku University) for helpful discussions. The technical assistance for the PET experiments by the members of the Research Institute of Brain and Blood Vessels, Akita, Japan, is also gratefully acknowledged.

Conflict of interest

No conflict of interest exists in connection with this article.